PAPER

Streamwise and lateral maneuvers of a fish-inspired hydrofoil

Bioinspiration & Biomimetics

PAPER

Streamwise and lateral maneuvers of a fish-inspired hydrofoil

Qiang Zhong[1,*] and Daniel B Quinn[1,2]

[1] Department of Mechanical and Aerospace Engineering, University of Virginia, Charlottesville, VA 22904, United States of America
[2] Department of Electrical and Computer Engineering, University of Virginia, Charlottesville, VA 22904, United States of America
[*] Author to whom any correspondence should be addressed.

E-mail: qz4te@virginia.edu

RECEIVED
28 April 2021

REVISED
18 July 2021

ACCEPTED FOR PUBLICATION
5 August 2021

PUBLISHED
24 August 2021

Keywords: unsteady fluid dynamics, fish inspired maneuver, bioinspiration

Supplementary material for this article is available online

Abstract

Fish are highly maneuverable compared to human-made underwater vehicles. Maneuvers are inherently transient, so they are often studied via observations of fish and fish-like robots, where their dynamics cannot be recorded directly. To study maneuvers in isolation, we designed a new kind of wireless carriage whose air bushings allow a hydrofoil to maneuver semi-autonomously in a water channel. We show that modulating the hydrofoil's frequency, amplitude, pitch bias, and stroke speed ratio (pitching speed of left vs right stroke) produces streamwise and lateral maneuvers with mixed effectiveness. Modulating pitch bias, for example, produces quasi-steady lateral maneuvers with classic reverse von Kármán wakes, whereas modulating the stroke speed ratio produces sudden yaw torques and vortex pairs like those observed behind turning zebrafish. Our findings provide a new framework for considering in-plane maneuvers and streamwise/lateral trajectory corrections in fish and fish-inspired robots.

1. Introduction

In terms of maneuverability, fishes vastly outperform human-made vehicles, especially at low speeds [1, 2]. In fact, maneuvering 'appears to have been a major factor in the evolution of the chordate body plan' [3]. The maneuverabilities found in nature are thought to stem from body/fin flexibility [4] and coordinated control surfaces [5]. However, due to the diversity and complexity of maneuvers and the limits on diagnostic methods, it remains unclear how the dynamics of maneuvering fins relate to force generation and asymmetric wakes.

One way to roughly categorize fish maneuvers is to separate them into streamwise (anterior–posterior) and lateral (left–right) maneuvers. Accelerating from rest is a streamwise maneuver; coordinating a turn is a lateral maneuver. Fish are effective at both maneuver types. Trout and pike can accelerate forward at 40 and 50 m s^{-2} [6]; goldfish have turning a radius less than their body length [7].

A simple way to produce a streamwise maneuver is to adjust the tailbeat amplitude and/or frequency. Sunfish [8] and lampreys [9], for example, increase their tailbeat amplitude when accelerating. This strategy is common: across 51 species spanning 20 taxonomic orders, the tailbeat amplitude increases by 34 $\pm$4% during accelerations [10]. Once swimming steadily, a fish's speed is more often controlled by tailbeat frequency [10, 11].

To perform a lateral maneuver, fishes might break either their gait's spatial or temporal symmetry. For example, one stroke of a fin could have a larger amplitude than another stroke (spatial asymmetry) or be faster than another stroke (temporal asymmetry). These asymmetries can be small, producing quasi-steady 'trimming forces' [12, 13], or large, producing 'powered correction forces' that drive unsteady flows and rapid maneuvers [5]. Our understanding of these strategies comes from applying aerodynamic intuition to biological observations: e.g. trimming forces are thought to be more efficient but only at high speeds [14].

While most bio-inspired propulsion studies have focused on symmetric motions [15], a few have considered maneuvers. For example, energy and force analyses have been based on the flow fields around turning zebra fish [16]. High-fidelity simulations have been used to study larval fish and their three-dimensional wakes during a 'C start' (a combination of spatial and temporal asymmetry) [17]. Studying real fish ensures high fidelity, but it cannot produce

prescribed kinematics, which are helpful for systematic multi-trial maneuver studies. It also introduces several independent variables due to the complexity of a fish's kinematics and morphology.

An indirect but effective way of studying fish maneuvers is to characterize the dynamics of autonomous fish-inspired robots. Adding a pitch offset (spatial asymmetry) to a robotic tail fin has been used to study lateral maneuvers in salmon-like [18] and tuna-like [19] robots. Flapping faster in one direction than the other (temporal asymmetry) has been used to study maneuvers in tuna-like robots up to high frequencies [20]. A challenge of these studies is that robot efficiencies are estimated using noisy battery drain data, and precise force measurements cannot be done on untethered platforms. Wake studies are also limited by the difficulty of performing flow visualization on a moving target.

A third method of studying maneuvers is to use tethered fish-inspired platforms. Tethered platforms have revealed, for example, the role that flexibility and C-start kinematics play in rapid streamwise maneuvers [21–24]. In a study of pitch-biased (spatially asymmetric) hydrofoil, researchers showed that pressure sensors could inform a lateral maneuver in a vortex street [25]. In another pitch-bias study, researchers recorded lateral force coefficients (lateral forces scaled by foil area and dynamic pressure) up to 5.5, suggesting rapid lateral maneuvers could result from pitch bias [26]. A limitation of these studies is that they do not allow recoil or at least restrict recoil to one axis using linear air bushings.

For this study, we designed a semi-autonomous rig that has some elements of autonomous robots and some of tethered platforms. Our goal was not to replace either but rather to capitalize on some benefits of both. We suspended an oscillating hydrofoil from two axes of air bushings to allow both streamwise and lateral recoils during fish-inspired maneuvers. Our rig cannot reproduce the 3D dynamics of fully autonomous propulsors, but it offers precise force and flowfield measurements for propulsors freely recoiling in two directions. We present results for two streamwise and two lateral maneuver types: (1) an increase in amplitude, (2) an increase in frequency, (3) an increase in spatial asymmetry, and (4) an increase in temporal asymmetry. For each maneuver type, we quantify the dynamics and the surrounding flowfield, then discuss their implications for fish and fish-inspired robot maneuvers.

2. Experimental methods

2.1. A wireless carriage with a pitching hydrofoil

To study the dynamics of maneuvers, we suspended an oscillating hydrofoil from a wireless carriage that slides freely in a horizontal plane (figure 1(a)). To align our setup with our previous work, we used a 3D-printed teardrop-shaped hydrofoil with a chord (c) of 95 mm and span (w) of 143 mm (aspect ratio 1.5). The hydrofoil swam in a closed-loop water channel with a L: 1520 mm $\times$ W: 380 mm $\times$ H: 450 mm test section. An incoming flow speed of $u = 300$ mm s^{-1} was regulated by a custom circuit (Arduino Mega with a signal amplifier) and an ultrasonic flow sensor (Dynasonics Series TFXB). The carriage and its supporting frame consisted of three major subsystems: a two-axis air suspension system, a pitch actuator, and an automated tilting system.

Two-axis air suspension system. Two sets of steel rails supported the carriage: an outer frame supported two rails spanning the streamwise axis, and an inner frame supported two rails spanning the lateral axis (figure 1(b)). Seven air-bushings (S303901, New Way Air Bearings. Inc.) (three on lateral axis rails and four on streamwise axis rails) allowed the carriage to glide in a horizontal plane. The carriage's effective mass was 4.6 kg in the lateral direction (without the streamwise axis rails and support frames) and 13.6 kg in the streamwise axis direction.

To minimize outside influences on the carriage's motions, we designed the carriage to be fully untethered. The carriage housed a wireless receiver (Arduino Mega 2560 with Xbee shield), a wireless transmitter (ATI F/T wireless), a power source (16.8 V LiPO battery), and two compressed air tanks (Ninja HPA Tank—68 CI—4500 PSI) to run the air bushings. The carriage's in-plane position ($S(t)$, $L(t)$) was captured by onboard laser distance sensors (Baumer C8501) with $\pm$0.05 mm resolution for the streamwise position ($S(t)$) and $\pm$0.01 mm for the lateral position ($L(t)$). Airflow to the bushings was controlled by digital-controlled solenoid valves. To avoid time delay between the measured signals, we used a custom onboard circuit to synchronize measurements before transmitting wirelessly to the control PC.

We quantified the small but nonzero friction in the air bushings using a separate test. We pushed the carriage gently by hand with a small initial velocity, then measured the carriage's position as it came to rest. We then extracted the average deceleration value and multiplied it with carriage mass to estimate friction force. Tests were performed at least five times from each side of the rail to improve measurement accuracy. The average resistance force was 0.0017 $\pm$ 0.0007 N on the lateral axis and 0.036 $\pm$ 0.012 N on the streamwise axis.

To maximize the repeatability of the maneuver trials, we used an automated carriage reset system (figure 1(e)). The reset system used a horizontal traverse to automatically align a servo-controlled gripper with the L position of the hydrofoil (as recorded by the laser distance sensor on the carriage). In between trials, the gripper brought the hydrofoil back to its starting position. The reset system

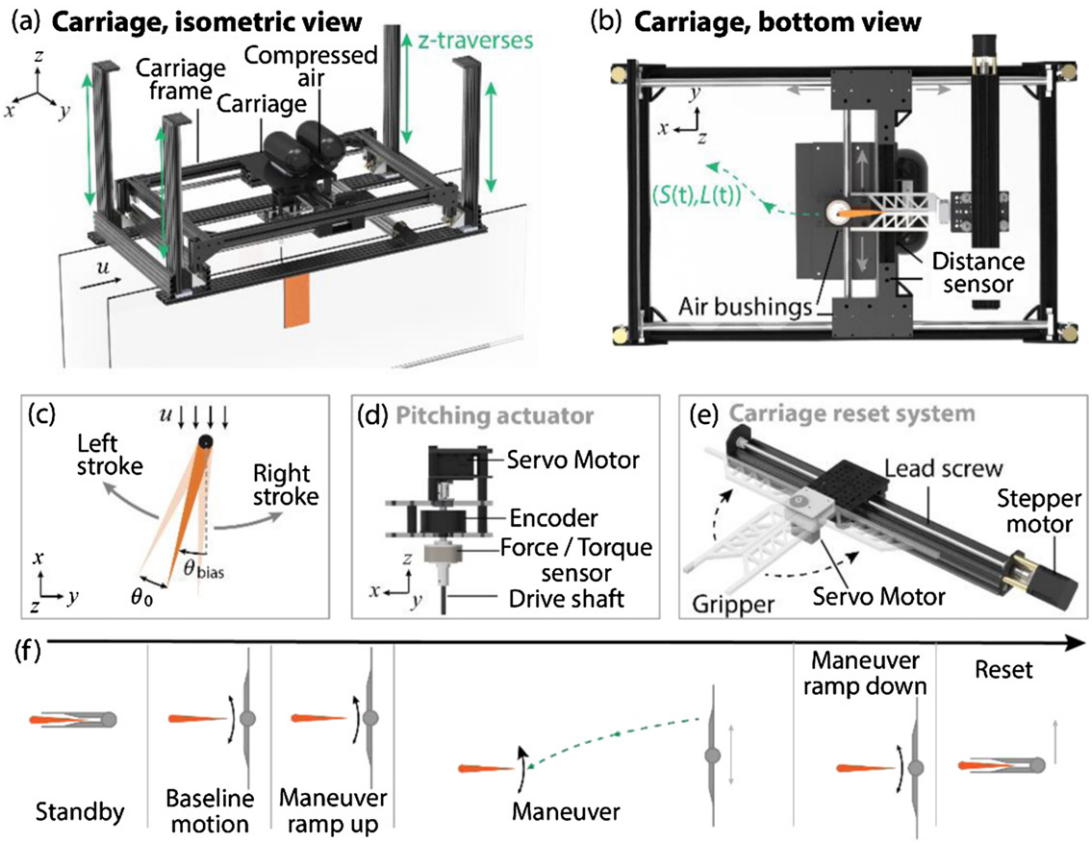

Figure 1. A wireless experimental rig for studying bio-inspired maneuvers. (a) A carriage gliding on air bushings suspended a hydrofoil into the center of a water channel. Four stepper motors (z-traverses) auto-level the carriage frame. (b) Seven air bushings provide the carriage with streamwise and lateral freedom. (c) Definition of pitching motion and asymmetry direction. (d) Pitching motions are generated by a servo motor; driveshaft dynamics are recorded by a force/torque sensor and encoder. (e) The carriage reset system uses a linear actuator and a servo-driven gripper to reset the carriage in between trials. (f) Visualization of a maneuver test trial. Each step was performed automatically by an online control PC. See supplementary material (https://stacks.iop.org/BB/16/056015/mmedia) for more details and design files.

allowed maneuver tests that were autonomous yet repeatable.

Pitch actuator. To measure the force precisely, the hydrofoil was connected to a six-axis force/torque sensor (ATI Inc., Mini-40), then pitched by an actuator installed on the bottom of the carriage (figure 1(d)). The actuator used a high torque digital servo motor (Dynamixel MX-64) to transmit motion to the hydrofoil via a carbon fiber driveshaft ($\emptyset = 6.35$ mm). An absolute encoder (US Digital A2K 4096 CPR; resolution: $\pm 0.01^\circ$) recorded the actual angle of the driveshaft for use in later calculations.

Automated tilt system. The automated tilt system used four stepper motors to raise/lower the four corners of the carriage support frame independently (figure 1(a)). These motors auto leveled the carriage to $\pm 0.001^\circ$ precision, which reduced the effects of gravity during maneuver to < 2.5 mN.

2.2. Streamwise/lateral maneuvers

To parameterize the hydrofoil maneuvers, we used inverse trig functions to create a family of pitch angle functions that capture the four maneuver types we studied. Using our approach, pitch angle is prescribed as

$$\theta(t) = \theta_{\text{bias}} + \theta_0 \frac{\tan^{-1}\left(\frac{\zeta \sin 2\pi f t}{1-\zeta \cos 2\pi f t}\right)}{\tan^{-1}\left(\frac{\zeta}{\sqrt{1-\zeta^2}}\right)},$$

where θ_0 is pitching amplitude, f is pitching frequency, θ_{bias} is pitch bias angle, and ζ is stroke speed ratio. The bias angle, θ_{bias}, sets the average pitch angle within an oscillation cycle and initiates lateral maneuvers via spatial asymmetry. The stroke speed ratio, ζ, sets the difference between pitch velocities of left and right strokes. As $\zeta \to 0$, $\theta(t)$ approaches a sine wave; as $\zeta \to 1$, $\theta(t)$ approaches a sawtooth wave.

We chose a range of maneuver parameters based on our system's performance limits and observations from biology (table 1). We chose a symmetric motion as a baseline case with a moderate Strouhal number ($\theta_0 = 10^\circ, f = 1.5$ Hz, $\theta_{\text{bias}} = 0$, and $\zeta = 0$; $\text{St} = 2fc \sin\theta_0/u = 0.165$). With those baseline kinematics, the hydrofoil produced just enough thrust to offset the incoming flow ($u = 300$ mm s^{-1}), meaning there were negligible streamwise and lateral displacements even when the hydrofoil's carriage was free to move on the air bushings. Maneuvering motions were defined in relation to this baseline motion. For

Table 1. Maneuver acceleration and velocity specs.

Maneuver direction	Parameters		Values						
Streamwise		θ_0 (degree)	10	12		14	16		18
	Amplitude modulation	$\ddot{S}_{\text{fit}}\frac{1}{2}$ (c/s^2)	0	0.0004		0.0024	0.0056		0.0086
		f (Hz)	1.5	1.75	2	2.25	2.5	2.75	3
	Frequency modulation	$\ddot{S}_{\text{fit}}$ (c/s^2)	0	0.0105	0.0232	0.0378	0.0539	0.0709	0.0991
Lateral		θ_{bias} (degree)	0	1	1.5	2	2.5	3	
	Spatial asymmetry	$\dot{L}_{\text{fit}}(c/s)$	0	0.31	0.47	0.65	0.78	0.92	
		ζ	0	0.15	0.3	0.45	0.6	0.75	0.9
	Temporal asymmetry	$\dot{L}_{\text{fit}}$ (c/s)	0	0.06	0.16	0.30	0.42	0.50	0.47

example, in a test that considered a stroke speed ratio $\zeta = 0.9$, the rest three parameters kept the same value as the baseline case ($\theta_0 = 10°, f = 1.5$ Hz, $\theta_{\text{bias}} = 0$). For all tests, the pitching motions started with a right stroke (figure 1(c)).

All maneuver tests started from steady swimming. Each trial started with the gripper of the carriage reset system releasing the hydrofoil in the center of the test section. Simultaneously, the hydrofoil started three cycles of the baseline symmetric motion. Next, the hydrofoil performed three cycles that smoothly vary from the baseline motion to the maneuvering motion. This 'maneuver ramp up' phase was followed by the 'maneuver', which consisted of ten pitching cycles of the asymmetric kinematics. After the maneuver was complete, three extra cycles were performed to vary from asymmetric kinematics back to the baseline motion smoothly. Large pitch angles were then introduced to amplify drag and push the hydrofoil back to where it could be intercepted by the gripper of the carriage reset system. Finally, the reset system brought the hydrofoil back to its starting position, and the process repeated (figure 1(f)). We repeated each test condition five times.

2.3. Performance metrics and flow fields

We quantified the performance of the hydrofoil based on its kinematic response and the forces it exerted on the water. Kinematics ($S(t)$ and $L(t)$) were recorded with the laser distance sensors, and forces were recorded with a six-axis force/torque sensor in line with the driveshaft. The resolutions of the force/torque sensor were sufficient to resolve the differences between trials: force resolution was ± 0.01 N along the streamwise and lateral axes, and the torque resolution was ± 0.25 Nmm. In this study, we reported results in non-dimensional form. The measured displacements were normalized by hydrofoils' chord length (c), and the thrust (F_{T}), lift (F_{L}) forces were normalized by the dynamic pressure and hydrofoil area:

$$C_{\text{T}} \equiv \frac{F_{\text{T}}}{\frac{1}{2}\rho u^2 cw}, \quad \text{and} \quad C_{\text{L}} \equiv \frac{F_{\text{L}}}{\frac{1}{2}\rho u^2 cw},$$

where ρ was the density of the fluid medium (water).

Because previous studies have considered the wakes of pitching hydrofoil with varying amplitudes and frequencies [27, 28], we chose to focus our wake study on lateral maneuvers. We quantified the wake with particle image velocimetry (PIV) performed at the mid-span of the hydrofoil. The flow was seeded with neutrally buoyant polyamide particles (PSP, $\emptyset \approx 20$ μm). A pair of continuous lasers (MGL-W-532, Raypower, and MGL-W532A, CNI) were fired from opposite sides to generate an overlapping laser sheet that illuminated particles without a shadow around the foil. Particle motions were recorded by two cameras (Phantom, SpeedSense M34; 2956 × 1877 px resolution) installed beneath the channel. The flow field analysis was performed by an adaptive PIV algorithm (Dantec Dynamic Studio 6.1) with a 32 × 32 px grid step size. When reporting vorticity and velocity plots, we phase-averaged 25 pitching cycles over 1000 frames. Phase-averaging was done in Matlab (2018a), and vorticity/velocity plots were created in Tecplot (2017R2).

3. Results

3.1. Bulk performance of streamwise maneuvers

We first consider the bulk performance of streamwise maneuvers, i.e. the general dynamics of the hydrofoil over the ten pitching cycles of the maneuver. As expected, increasing frequency and amplitude both led to streamwise displacements (figure 2(b)). The total displacements due to increasing frequency tended to be much larger than those due to increasing amplitude. For example, increasing frequency to 2.75 Hz caused a streamwise displacement of $1.19 \pm 0.07c$. Producing a similar Strouhal number (St ≈ 0.3) by increasing amplitude ($f = 1.5$ Hz; $\theta_0 = 18°$) only caused a streamwise displacement of 0.27 ± 0.03 c.

In addition to causing higher displacements, the frequency-driven maneuvers took less time. This combination led to much larger accelerations. To quantify the accelerations, we fitted parabolas to the streamwise position functions ($0.5\ddot{S}_{\text{fit}}t^2 + \dot{S}_{\text{fit}}t$, where $\ddot{S}_{\text{fit}}$ and $\dot{S}_{\text{fit}}$ are fitted constants; see table 1). The second term of the fit ($\dot{S}_{\text{fit}}t$) represents a potentially small but nonzero initial velocity at the start of the 'maneuver' phase. The success of the fit ($R^2 > 0.95$; figure 2(c)) shows that accelerations were roughly constant in magnitude. The magnitude of the acceleration scaled quadratically with

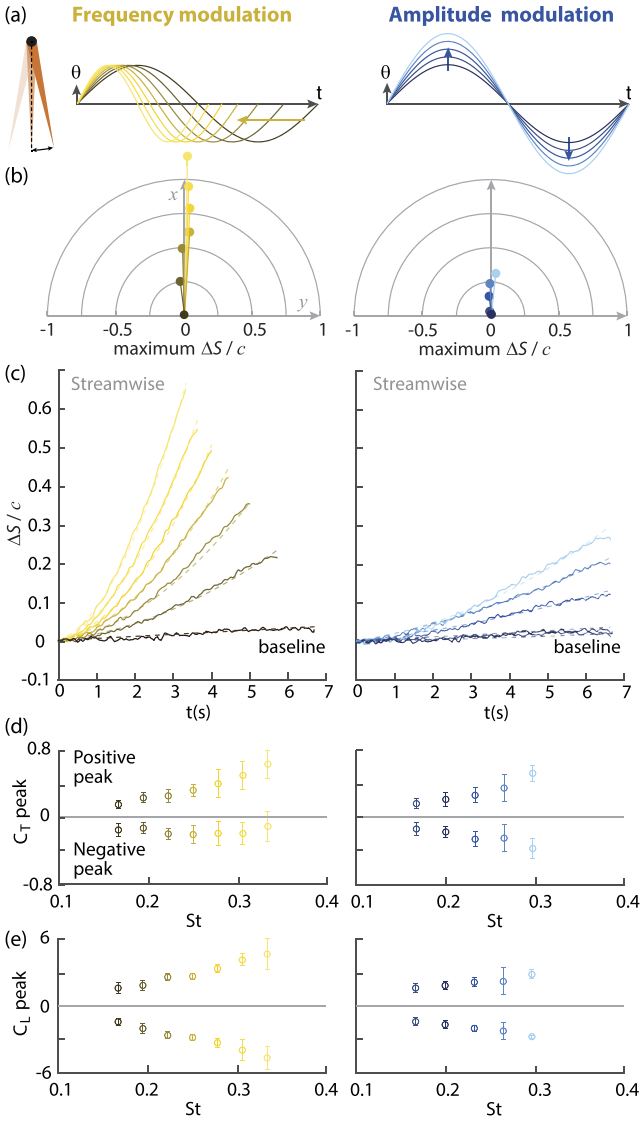

Figure 2. Bulk performance of streamwise maneuvers. (a) Pitching angle profiles of frequency and amplitude modulation cases. (b) Total displacement in streamwise and lateral directions after the ten-cycle maneuver. (c) Time-history of streamwise displacement during the maneuver. Solid lines: Measured raw data averaged over five independent trials, error bars are omitted for cleanliness; dash lines: fitted parabolas. (d) Averaged streamwise force peak magnitudes. (e) Averaged lateral force peak magnitudes. Error bars represent the standard deviation from mean ($N = 50$).

frequency ($\ddot{S}_{\text{fit}} = \left(0.014f^2 - 0.034\right) c/s; R^2 = 0.98$). These results corroborate scaling laws for thrust generation based on tethered experimental data [29, 30]. The magnitude of the acceleration also increased with amplitude, but no clear scaling trend was found.

Frequency-driven maneuvers—when compared with amplitude-driven maneuvers—also led to higher streamwise velocities ($\dot{S}$) at the end of the maneuvers (figure 2(c)). As a result, the hydrofoil coasted further after the 10-cycle maneuver was complete (figures 2(b) and (c)). In the frequency-driven case, these post-maneuver displacements were often comparable to the displacements of the maneuver itself.

In addition to recording displacements, we also recorded the peak magnitudes of streamwise and lateral forces. Increasing frequency led to higher positive peaks in streamwise force but had little effect on negative peaks in streamwise force (figure 2(d)). In contrast, increasing amplitude accentuated both the positive and negative peaks in streamwise force, presumably due to the increased projected area caused by higher amplitudes ($c \cdot w \cdot \sin\theta_0$). As for lateral forces, positive and negative peaks increased monotonically with Strouhal number and increased faster with increasing frequency. At St ≈ 0.3, increasing frequency to 2.75 Hz led to lateral force peaks about 1.7 times higher than the peaks brought on by increasing amplitude to $\theta_0 = 18°$. ($|C_L| = 4.7$ vs 2.8). Because the pitching motion was symmetrical for these streamwise maneuvers, the positive and negative peaks of the lateral force remained symmetrical.

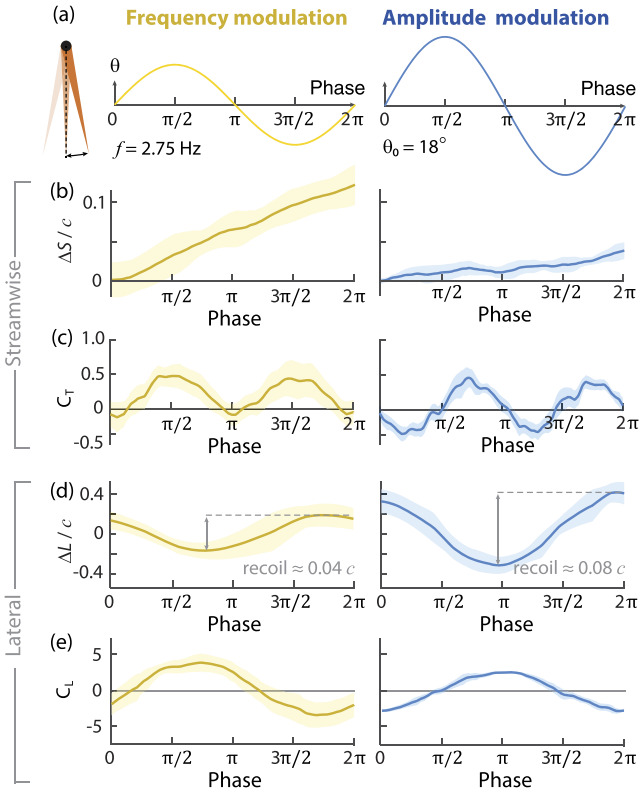

Figure 3. Intracycle dynamics of streamwise maneuvers. Curves and shaded bands represent the mean and standard deviation across five trials of the 5th pitching cycle of the maneuver. (a) Pitching angle profiles of one cycle. (b) Streamwise displacement. (c) Streamwise force coefficient. (d) Lateral displacement. Recoil was defined as peak to peak lateral displacement within one cycle. (e) Lateral force coefficient.

3.2. Instantaneous forces during streamwise maneuvers

The dynamics within a pitching cycle offer more details about the streamwise maneuvers. To compare instantaneous dynamics of the frequency-driven and amplitude-driven maneuvers, we compared two cases at a comparable Strouhal number ($f = 2.75$ Hz, $\theta_0 = 10°$ vs $f = 1.5$ Hz, $\theta_0 = 18°$; St ≈ 0.3). To avoid start and end effects, we compared the middle (5th) cycle of the ten-cycle maneuver averaged over the five trials.

On a per cycle basis, the frequency-driven maneuver produced more streamwise displacement than the amplitude-driven maneuver $0.126c$/cycle vs $0.04c$/cycle; figure 3(b)). These displacements correspond to average streamwise velocities of $0.35c$/s and $0.06c$/s. Instantaneous forces offer more details about the trends observed in the bulk performance of streamwise maneuver (figures 2(d) and (e); figures 3(c) and (e)). Increasing frequency caused higher positive peaks in streamwise force, with negative streamwise forces (drag) only appear in two brief periods of the pitching cycle (figure 3(c)). In comparison, increasing amplitude led to higher streamwise force peaks and lower negative peaks. The streamwise force reached its negative peak as the hydrofoil passed its midline and is approaching its maximum pitching angle (phase between $n\pi$ and $n\pi + \pi/2$).

Instantaneous kinematics also revealed that lateral recoil is more significant for amplitude-driven maneuvers than those of frequency-driven maneuvers. While lateral recoil was almost constant with increasing frequency, it increased considerably with amplitude. The peak-to-peak lateral displacement (ΔL) was $0.04c$ for the $f = 2.75$ Hz case but $0.08c$ for the $\theta_0 = 18°$ case (figure 3(d)). For comparison, peak-to-peak lateral displacement was $0.042c$ for the baseline kinematics. However, the lateral force peaks were actually higher in the frequency-driven maneuvers (figure 3(e)). This apparent contradiction might be due to the shorter cycle period of the frequency-driven maneuvers. Lateral forces scale with lateral acceleration ($\ddot{L}$), and lateral displacements scale with lateral acceleration times the square of the period ($\ddot{L} \cdot f^{-2}$). Frequency-driven maneuvers had higher lateral accelerations (figure 2(c)), but those accelerations scaled with f^2 and therefore led to comparable lateral displacements.

3.4. Bulk performance of lateral maneuvers

We now consider the bulk performance of the lateral maneuvers. As expected, both spatial and temporal asymmetries led to lateral displacements (figure 4(b)). Spatial asymmetries tended to cause larger total displacements (e.g. $\Delta L = 1.0c$ for $\theta_{\text{bias}} = 3°$ vs $\Delta L = 0.52c$ for $\zeta = 0.9$). In the case of spatialasymmetry, the fitted lateral maneu-

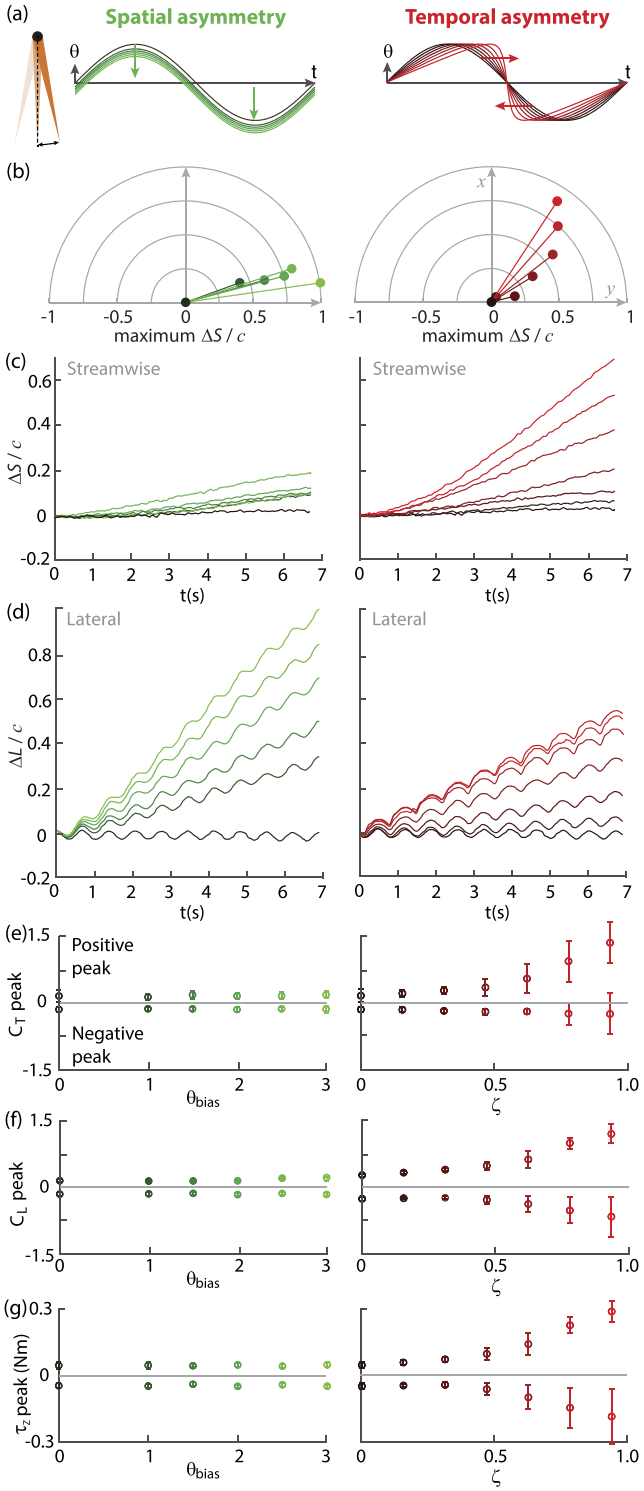

Figure 4. Bulk performance of lateral maneuvers. (a) Pitching angle profiles of spatial and temporal asymmetry cases. (b) Total displacement in streamwise and lateral directions after the ten-cycle maneuver. (c), (d) Time-history of streamwise and lateral displacement during the maneuver. Solid lines: measured raw data averaged over five independent trials. (e) Averaged streamwise force peak magnitudes. (f) Averaged lateral force peak magnitudes. (g) Averaged yaw axis torque peak magnitudes. Error bars represent the standard deviation from mean ($N = 50$).

ver speed increased linearly with pitch bias ($\dot{L}_{\text{fit}} = (0.31\theta_{\text{bias}})c/s$; $R^2 = 0.99$). In the case of temporal asymmetry, lateral displacement increased with stroke speed ratio but with no discernable closed-form scaling.

Temporal asymmetries also caused considerable streamwise displacements. Despite the maneuvers' defining feature being lateral asymmetry, the streamwise displacement was at times comparable to the lateral displacement. When $\zeta = 0.9$, for example,

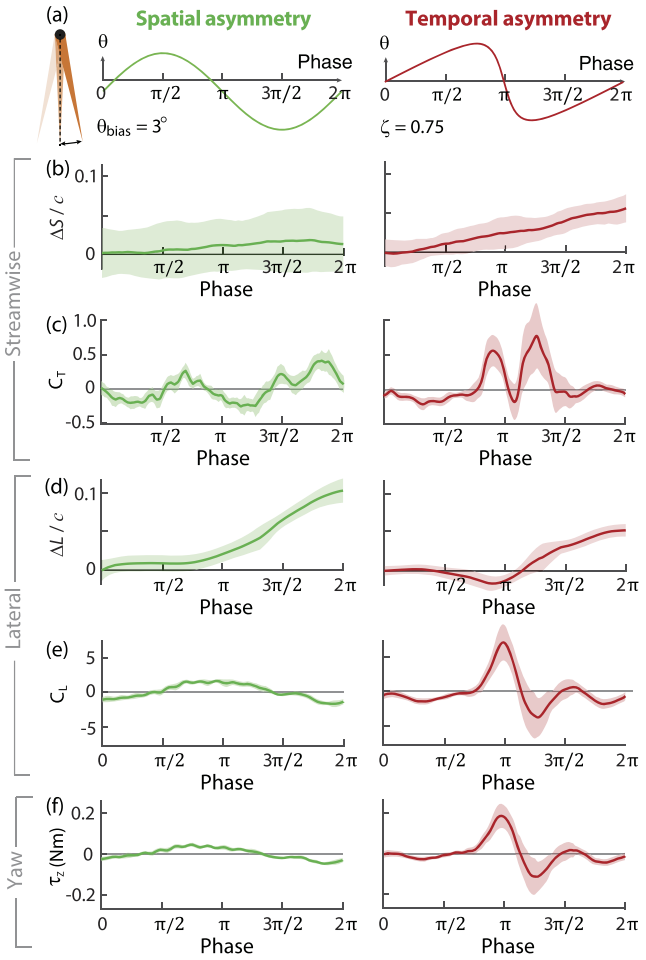

Figure 5. Intracycle dynamics of lateral maneuvers. Curves and shaded bands represent the mean and standard deviation across five trials of the 5th pitching cycle of the maneuver. (a) Pitching angle profiles of one cycle. (b) Streamwise displacement. (c) Streamwise force coefficient. (d) Lateral displacement. (e) Lateral force coefficient. (f) Yaw axis torque.

the displacement was higher in the streamwise direction than in the lateral direction ($\Delta S = 0.8 \pm 0.07c$; $\Delta L = 0.52 \pm 0.02c$).

Unlike the streamwise maneuvers, especially frequency-driven acceleration, where streamwise velocity steadily increased, lateral maneuvers produced nearly constant bulk lateral velocities (figure 4(d)). These lateral velocities increased with pitch bias angle (θ_{bias}) and stroke speed ratio (ζ), though they leveled off beyond a critical stroke speed ratio of about 0.6. Lateral recoil was relatively unaffected by θ_{bias} but increased with stroke speed ratio.

The differing streamwise and lateral force peaks further illustrate the differences between temporal and spatial pitching asymmetries. As θ_{bias} increased, streamwise and lateral force peaks stayed the same, even at the largest θ_{bias} value (figures 4(e) and (f)). As ζ increased, negative streamwise force peaks remained relatively unchanged, but positive streamwise force peaks rose considerably (figure 4(e)). Increasing ζ also led to a sharp increase in the magnitude of positive and negative lateral force peaks (figure 4(f)).

Because we merged the control surface and the propulsor into one device, our hydrofoil did not have the yaw freedom that a fully untethered hydrofoil would experience. However, measurements of yaw torque provide clues as to what a free hydrofoil's yaw response might be. Because the yaw torque was highly correlated with lateral force, we observed the same trends in yaw torque as in lateral force (figures 4(f) and (g)). The large differences between positive and negative yaw peaks suggest that a free hydrofoil would be more unstable in yaw in the temporal asymmetry case compared to the spatial asymmetry case.

3.5. Instantaneous forces during lateral maneuvers

The dynamics within a pitching cycle offer more details about the lateral maneuvers. As a representative comparison, we compared the $\theta_{\text{bias}} = 3°$ and $\zeta = 0.75$ cases (figure 5), but the same qualitative conclusions can be drawn from any pair of our spatial and temporal maneuvers. As before, we compared the middle (5th) cycle of the ten-cycle maneuver averaged over the five trials.

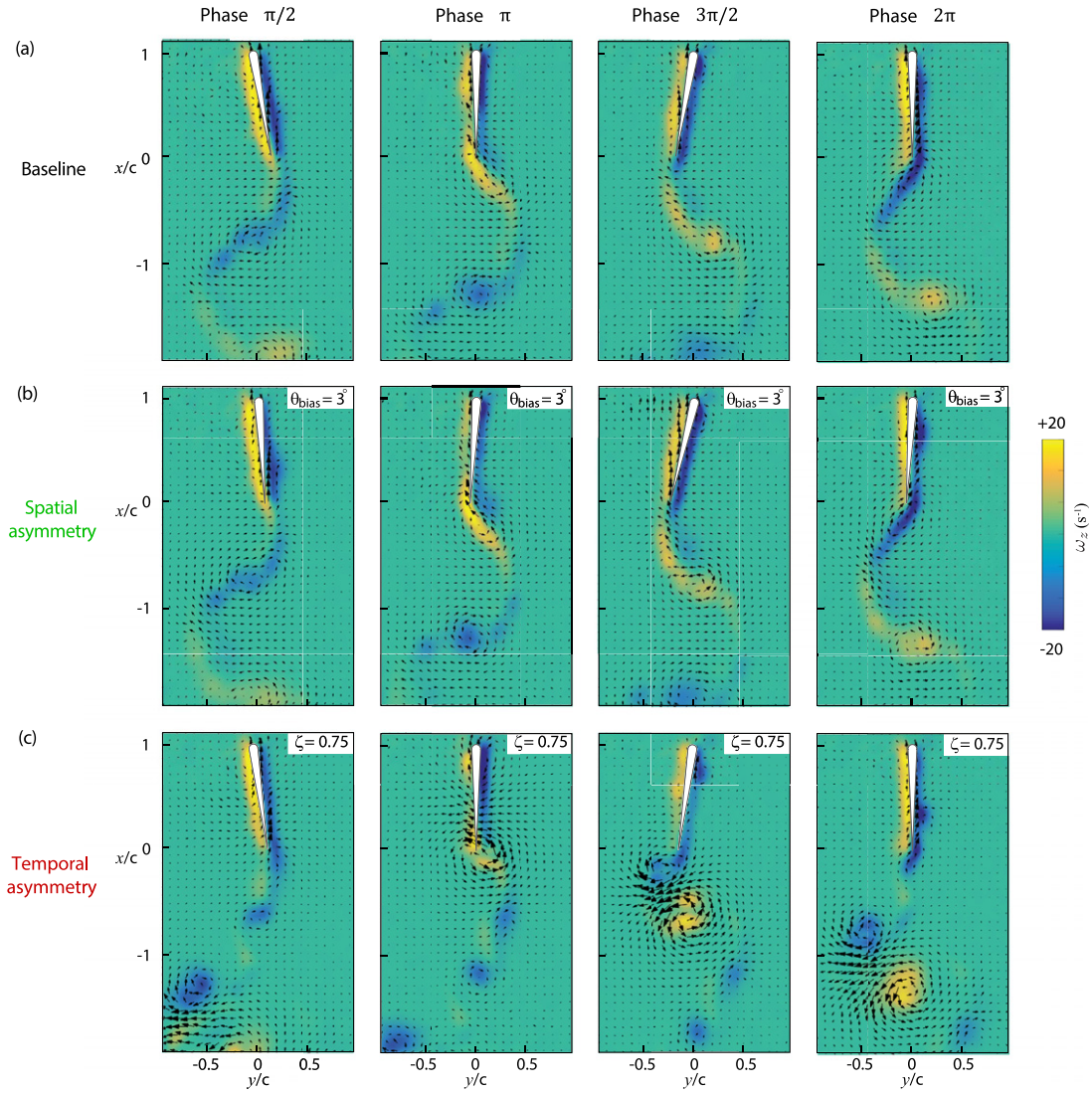

Figure 6. Flow field during lateral maneuver. Time sequence of the velocity (arrows) and z-vorticity (ω_z, background color) fields around the hydrofoil (white) of (a) free-swimming (baseline), (b) representative spatial asymmetry case ($\theta_{\text{bias}} = 3°$) and (c) representative temporal asymmetry case ($\zeta = 0.75$). In all cases, incoming flow speed was subtracted from the velocity fields. Each column shows one phase: first column: phase $= \pi/2$; second column: phase $= \pi$; third column: phase $= 3\pi/2$; fourth column: phase $= 2\pi$.

As expected based on bulk displacements (figure 4(b)), lateral maneuvers caused small streamwise displacements within each pitching cycle ($\Delta S = 0.02c$ for $\theta_{\text{bias}} = 3°$ vs $0.05c$ for $\zeta = 0.75$, figure 5(b)). Streamwise forces were larger in the second half of the pitching cycle (figure 5(c)), presumably because the higher pitch angle projected more lift force into the streamwise direction. Streamwise forces in the temporal asymmetry case show a very different pattern. Two large force peaks appear in the middle of the pitching cycle about 0.4π apart in-phase (figure 5(c)). This burst in streamwise force mid-cycle helps to explain the larger streamwise displacements caused by temporal asymmetry.

Spatial asymmetry also lead to smoother lateral maneuvers, whereas temporal asymmetries lead to more lateral recoil within each pitch cycle. In the spatial asymmetry case, the pitch bias shifts the lateral force slightly (figure 5(e)), causing a smooth, monotonic lateral displacement within the cycle (figure 5(d)). As for temporal asymmetry, the hydrofoil generates a strong positive lateral force, then a negative lateral force, over a short time (phase $\approx 0.75\pi$ to 1.5π, figure 5(e)). The result is a jerkier lateral displacement, including a short period of negative lateral displacement (figure 5(d)).

As with the spatial asymmetries, the yaw torque (τ_z) showed a similar trend as the lateral force. Adding spatial asymmetry introduces small perturbations to yaw torque, whereas adding temporal asymmetry introduces large positive and negative peaks in yaw torque, presumably with implications for yaw stability in the case of a fully untethered hydrofoil.

3.6. Wake structures behind lateral maneuvers

Because the wakes behind symmetric pitching motions have been studied previously (e.g. [27, 28]), we focused on characterizing the flowfield behind the

laterally maneuvering hydrofoils. As a control case, we considered the wake produced by the baseline kinematics. This symmetric motion produces a classic reverse von Kármán vortex street, with each vortex shed at roughly the moment of maximum pitch angle (figure 6(a)).

Despite the symmetric kinematics in the baseline case, the vortex street was not perfectly symmetric about the centerline of the water channel (centerline $y/c = +0.05c$ at phase π, $y/c = +0.2c$ at phase 2π). Asymmetric wakes generated by symmetric motions have been observed previously and have been attributed to wake instabilities that are sensitive to initial pitch direction and Strouhal number [31, 32]. However, deflected vortices caused by wake instability only appear at high Strouhal numbers and are usually absent behind finite aspect ratio hydrofoils [33]. It is therefore more likely that a slight misalignment caused the angled vortex street in the control case (figure 6(a)). Regardless of its origin, the angle does not affect our conclusions, because we consider here the relative effects of adding asymmetry.

When spatial asymmetry was added via a pitch bias angle, the wakes are vectored in the direction of the pitch bias. We found that both positive and negative vortices are shifted toward in the pitch bias direction by $0.15c$ compared to the baseline case ($y/c = -0.1c$ at phase π, $y/c = +0.05c$ at phase 2π). Other than this slight deflection, the wake structure was indistinguishable from the vortex street of the baseline case. The similarity to the baseline case is likely due to the small values of pitch bias considered here ($\leqslant 3°$). At sufficiently high values of pitch bias, the wake is bound to deviate from the baseline case.

Adding temporal asymmetry introduced drastic changes in the wake behind the hydrofoil. When the hydrofoil pitches through the midline (phase π), a strong trailing edge vortex appears and grows for the rest of the stroke (figure 6(c), from phase $\pi/2$ to phase π). This vortex may help to explain the high-magnitude pulse in lateral force at that same phase (figure 5(e)). As the hydrofoil reaches its maximum pitch angle, it shed this strong positive vortex. Then, as the hydrofoil slowly pitches the other way, a negative vortex is shed from the hydrofoil's trailing edge. Together with the positive vortex, this pair of vortices generated a strong jet in the left-rear direction of the hydrofoil (figure 6(c), phase $3\pi/2$ to phase 2π). This paired vortex wake topology is a significant deviation from the classic vortex street of the baseline case.

4. Discussion and conclusion

An increase in either amplitude or frequency will increase the Strouhal number, which increases thrust [29, 30]. However, we found that at the same Strouhal number, a frequency-driven maneuver produces significant stronger acceleration compared to an amplitude-driven maneuver. This result could help explain why natural swimmers prefer to modulate their tail-beat frequency to adjust swimming speed [10]. Increasing frequency also led to less lateral recoil, which suggests greater lateral stability while accelerating. Because our hydrofoil has a fixed average yaw angle, our rig cannot confirm lateral instabilities, but real fish that modulate tail-beat amplitude during accelerations do show greater lateral recoil [8].

While our results suggest that frequency modulation is a better acceleration strategy, amplitude modulation has benefits. First, it could further increase the Strouhal number in cases where frequency was already maximized, leading to even faster accelerations. Second, amplitude can affect wake structure, which affects efficiency. In rainbow trout, for example, increasing amplitude can realign vortex pairs, causing a more efficient downstream-facing momentum jet [10]. Higher amplitudes also provide a rapid braking mechanism due to high drag forces [26]. In fact, it was this mechanism that we harnessed for the recovery phase of our maneuver tests.

Adding pitch bias (spatial asymmetry) creates smooth, quasi-steady lateral maneuvers. The fact that lateral displacement scales linearly with pitch bias suggests that those lateral maneuvers are driven by the quasi-steady lift term of thin airfoil theory [34]. These findings are in line with maneuvering studies of fish-inspired robots, where pitch bias caused smooth yaw motions [35]. A key advantage of pitch bias modulation is its mechanical simplicity. Several central pattern generator control-based robot fishes have deployed this simple strategy to perform large radius turning [18, 20]. Previous tethered hydrofoil studies reported that asymmetric lift force could be affected by Strouhal number as well as pitch bias. In both heaving [26] and pitching [36] foil studies, increasing Strouhal number led to a larger lateral force, suggesting that unsteady lift terms may play a role in pitch-modulated maneuvers at higher Strouhal numbers.

Larger values of pitch bias are likely to cause more aggressive maneuvers. Our study limited spatial asymmetries ($\theta_{bias} \leqslant 3°$) to avoid collision with the sidewalls. In experiments on tethered hydrofoils [26, 36], lift continued to increase with bias angle while thrust showed a noticeable decrease when bias angle was larger than $\approx 5°$. With sufficiently high pitch bias, thrust became negative (drag). A free-swimmer could potentially use high values of pitch bias to perform sharp braking and lateral maneuvers simultaneously.

Modulating stroke speed ratio (temporal asymmetry) creates lateral maneuvers that are more complex. First, the lateral asymmetry causes streamwise

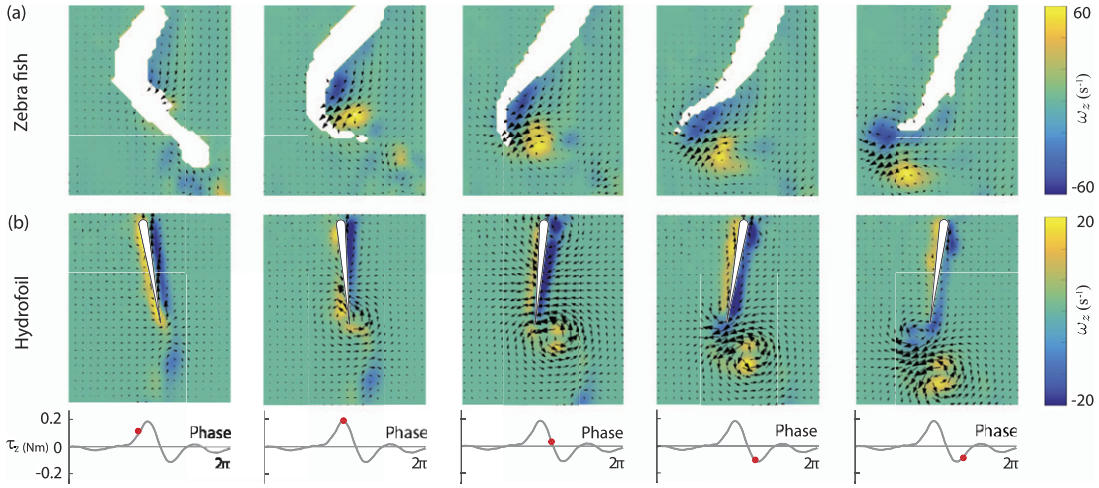

Figure 7. Flow field comparison between zebrafish turning and temporally asymmetric pitching. (a) Time sequence of the velocity (arrows) and z-vorticity (ω_z, background color) as zebrafish (white) perform a yaw maneuver. Body-based Re $= 2500 \pm 700$. Time between snapshots: 1/32 s. Reproduced from [37]. CC BY 4.0. (b) Time sequence of the velocity (arrows) and vorticity (background color) around the temporal asymmetric hydrofoil (white, $\zeta = 0.75$). Chord-based Re $= 28\,500$. Incoming flow speed was subtracted from the velocity fields for both cases. Bottom row: yaw torque (τ_z) as a function of phase; red dot indicates phase of PIV.

acceleration due to the higher mid-cycle lateral tail speeds. Fish and robots wanting to avoid this effect may want to reduce frequency and/or amplitude as they change stroke speed ratio. Fish can adjust both simultaneously: rainbow trout, for example, modulate their amplitude/frequency while swimming through a vortex street [12]. Introducing temporal asymmetry also leads to a paired vortex wake (figure 6(f)) and a burst of asymmetric yaw torque (figure 5(f)), which could presumably be used to rapidly reorient a fish or robot's yaw angle.

Because some fish use temporal asymmetry to produce yaw maneuvers, we compared our results with dynamics of turning zebrafish. The positive and negative peaks in lateral force that we observed (figure 5(e)) are qualitatively similar to lateral force estimates along the body of a turning zebrafish [16]. The flowfields around a turning zebrafish [37] also share some features with our PIV results (figure 7). During the yaw turn, the fish uses a fast leftward stroke to release a strong vortex pair into the wake. The caudal fin then sheds this vortex pair and the fish's body yaw angle shifts. Our PIV results also show a vortex pair shed around the moment of a sudden yaw torque (figure 7(b)). Other phases in the cycle show fewer similarities. Our hydrofoil is rigid, so it does not generate vorticity along a curled body as the fish does, and our hydrofoil's mean yaw position cannot react to the yaw torque. Still, the similarities suggest that at least some of the dynamics we observed can be used to better understand yaw reorientations in real fish.

In the context of fish-inspired robots, actuator constraints will dictate what maneuver types are feasible. Implementing actuation may cost more energy and increase the complexity of the robot, so choosing an asymmetry type is a critical design decision. For example, the Tunabot [39], in its current form, has one degree of freedom and performs straight-line swimming. Modulating frequency requires simple commands to the motor, whereas modulating amplitude would require a new actuator. Modulating the pitch bias angle would require yet another actuator, but modulating the stroke speed ratio could be done with a rotary encoder and a more advanced motor controller. Our semi-autonomous carriage for testing maneuvers offers a new method for characterizing these types of tradeoffs in bio-inspired propulsors. Our rig does has around 0.036 N of resistance force along the streamwise axis, which is negligible for larger-scale swimmers or high thrust cases but could reduce measurement accuracies for small-scale swimmers. For readers interested in replicating or modifying our setup, we uploaded all our design files—including those for the carriage reset system—as supplementary materials.

While we have focused on 'maneuvers', asymmetries are also relevant to slight corrections during steady swimming. Fish tend to be passively unstable in both yaw [3] and roll [38], so maintaining a stable attitude requires asymmetric kinematics even during normal swimming. Our results, therefore, offer a framework for streamwise/lateral corrections more generally. Whether a fish/robot intends to change trajectory or maintain the same trajectory, they can use a combination of streamwise and lateral modulations to achieve their goal.

Acknowledgments

This work was supported by the National Science Foundation (PI Daniel B Quinn and Keith W Moored,

Award No. 1921809; PI Daniel B Quinn, Award No. 2040351; Program Manager: R Joslin) and the Office of Naval Research (PI Daniel B Quinn, Award No. N00014-18-1-2537; Program Manager: B Brizzolara).

Data availability statement

All data that support the findings of this study are included within the article (and any supplementary files).

ORCID iDs

Qiang Zhong https://orcid.org/0000-0002-8435-5938
Daniel B Quinn https://orcid.org/0000-0002-5835-5221

References

[1] Bandyopadhyay P R 2002 Maneuvering hydrodynamics of fish and small underwater vehicles *Integr. Comp. Biol.* **42** 102–17
[2] Fish F E 2020 Advantages of aquatic animals as models for bio-inspired drones over present AUV technology *Bioinsp. Biomim.* **15** 025001
[3] Webb P W and Weihs D 2015 Stability versus maneuvering: challenges for stability during swimming by fishes *Integr. Comp. Biol.* **55** 753–64
[4] Fish F E 1999 Performance constraints on the maneuverability of flexible and rigid biological systems *Int. Symp. on Unmanned Untethered Submersible Technology* pp 394–406
[5] Fish F E and Lauder G V 2017 Control surfaces of aquatic vertebrates: active and passive design and function *J. Exp. Biol.* **220** 4351–63
[6] Weihs D 1973 The mechanism of rapid starting of slender fish *Biorheology* **10** 343–50
[7] Weihs D 1972 A hydrodynamical analysis of fish turning manoeuvres *Proc. R. Soc.* B **182** 59–72
[8] Wise T N, Schwalbe M A B and Tytell E D 2018 Hydrodynamics of linear acceleration in bluegill sunfish *L. macrochirus J. Exp. Biol.* **221** jeb190892
[9] Du Clos K T *et al* 2019 Thrust generation during steady swimming and acceleration from rest in anguilliform swimmers *J. Exp. Biol.* **222** jeb212464
[10] Akanyeti O, Putney J, Yanagitsuru Y R, Lauder G V, Stewart W J and Liao J C 2017 Accelerating fishes increase propulsive efficiency by modulating vortex ring geometry *Proc. Natl Acad. Sci. USA* **114** 13828–33
[11] Bainbridge R 1958 The speed of swimming of fish as related to size and to the frequency and amplitude of the tail beat *J. Exp. Biol.* **35** 109–33
[12] Liao J C, Beal D N, Lauder G V and Triantafyllou M S 2003 The Kármán gait: novel body kinematics of rainbow trout swimming in a vortex street *J. Exp. Biol.* **206** 1059–73
[13] Webb P W 2002 Control of posture, depth, and swimming trajectories of fishes *Integr. Comp. Biol.* **42** 94–101
[14] Blake R W 1979 The energetics of hovering in the Mandarin fish (*S. picturatus*) *J. Exp. Biol.* **82** 25–33
[15] Wu X, Zhang X, Tian X, Li X and Lu W 2020 A review on fluid dynamics of flapping foils *Ocean Eng.* **195** 106712
[16] Thandiackal R and Lauder G V 2020 How zebrafish turn: analysis of pressure force dynamics and mechanical work *J. Exp. Biol.* **223** jeb223230
[17] Liu H, Li G, Müller U K and Van Leeuwen J L 2014 Escape trajectories are deflected when fish larvae intercept their own C-start wake *J. R. Soc. Interface* **11** 20140848
[18] Wu Z, Yu J, Tan M and Zhang J 2014 Kinematic comparison of forward and backward swimming and maneuvering in a self-propelled sub-carangiform robotic fish *J. Bionic Eng.* **11** 199–212
[19] Anderson J M and Chhabra N K 2002 Maneuvering and stability performance of a robotic tuna *Integr. Comp. Biol.* **42** 118–26
[20] Yu J, Zhang C and Liu L 2016 Design and control of a single-motor-actuated robotic fish capable of fast swimming and maneuverability *IEEE/ASME Trans. Mechatron.* **21** 1711–9
[21] Wen L *et al* 2018 Understanding fish linear acceleration using an undulatory biorobotic model with soft fluidic elastomer actuated morphing median fins *Soft Robot.* **5** 375–88
[22] Witt W C, Wen L and Lauder G V 2015 Hydrodynamics of C-start escape responses of fish as studied with simple physical models *Integr. Comp. Biol.* **55** 728–39
[23] Currier T and Modarres-Sadeghi Y 2019 An experimental model with passively variable stiffness to investigate the effect of body stiffness on the fish fast-start maneuver *Exp. Fluids* **60** 147–8
[24] Conte J, Modarres-Sadeghi Y, Watts M N, Hover F S and Triantafyllou M S 2010 A fast-starting mechanical fish that accelerates at 40 m s^{-2} *Bioinsp. Biomim.* **5** 035004
[25] Free B A and Paley D 2018 Model-based observer and feedback control design for a rigid Joukowski foil in a Kármán vortex street *Bioinsp. Biomim.* **13** 035001
[26] Read D A, Hover F S and Triantafyllou M S 2003 Forces on oscillating foils for propulsion and maneuvering *J. Fluids Struct.* **17** 163–83
[27] Koochesfahani M M 1989 Vortical patterns in the wake of an oscillating airfoil *AIAA J.* **27** 1200–5
[28] Schnipper T, Andersen A and Bohr T 2009 Vortex wakes of a flapping foil *J. Fluid Mech.* **633** 411–23
[29] Ayancik F, Zhong Q, Quinn D B, Brandes A, Bart-Smith H and Moored K W 2019 Scaling laws for the propulsive performance of three-dimensional pitching propulsors *J. Fluid Mech.* **871** 1117–38
[30] Floryan D, Van Buren T, Rowley C W and Smits A J 2017 Scaling the propulsive performance of heaving and pitching foils *J. Fluid Mech.* **822** 386–97
[31] Cleaver D J, Wang Z and Gursul I 2012 Bifurcating flows of plunging aerofoils at high Strouhal numbers *J. Fluid Mech.* **708** 349–76
[32] Liang C, Ou K, Premasuthan S, Jameson A and Wang Z J 2011 High-order accurate simulations of unsteady flow past plunging and pitching airfoils *Comput. Fluids* **40** 236–48
[33] Calderon D E, Cleaver D J, Gursul I and Wang Z 2014 On the absence of asymmetric wakes for periodically plunging finite wings *Phys. Fluids* **26** 71907
[34] Garrick I E 1936 Propulsion of a flapping and oscillating airfoil *Rep. Natl. Advis. Comm. Aeronaut. NACA Rep.* 419–27
[35] Mason R and Burdick J W 2000 Experiments in Carangiform robotic fish locomotion *Proc. IEEE Int. Conf. Robotica and Automation* vol 1 pp 428–35
[36] Gunnarson P, Zhong Q and Quinn D B 2019 Comparing models of lateral station-keeping for pitching hydrofoils *Biomimetics* **4** 51
[37] Mwaffo V, Zhang P, Cruz S R and Porfiri M 2017 Zebrafish swimming in the flow: a particle image velocimetry study *PeerJ* **2017** e4041
[38] Moyle P B and Cech J J 2004 *Fishes: An Introduction to Ichthyology* 5th edn (Englewood Cliffs, NJ: Prentice Hall)
[39] Zhu J, White C, Wainwright D K, Di Santo V, Lauder G V and Bart-Smith H 2019 Tuna robotics: a high-frequency experimental platform exploring the performance space of swimming fishes *Sci. Robot.* **4** eaax4615